Original Research Article

Mechanical behavior and fracture analysis of sandstone containing cross-fissures under uniaxial compression by digital image correlation

Yuanyuan Wan, Xiangru Liu, Xuelei Zhang

School of Architecture and Civil Engineering, Suqian University, Suqian, 233800, People's Republic of China

Abstract: To investigate the mechanical behavior and cracking process of fissured rock, uniaxial compression tests were conducted on sandstone specimens containing cross-fissures. During the experiments, crack initiation, propagation and coalescence were monitored by using acoustic emission (AE) method and digital image correlation (DIC) technique. Experimental results indicate that the ligament angle is a significant factor influencing the mechanical behaviors of pre-cracked specimen. With an increase of ligament angle, the peak strength and peak strain first increase, and then decrease, finally increase again, whereas the elastic modulus first decreases and then increases. Based on the analysis of the ultimate failure patterns, rock bridge coalescence mode can be classified into five categories: no coalescence, shear coalescence, tensile coalescence, three-shear coalescence and double-tensile coalescence. AE counts reach the maximum value at or after the peak strength. Additionally, the evolution of the strain localization zone can be used for identification of cracking processes, namely crack initiation, propagation and coalescence.

Keywords: Fissured rock; Mechanical behavior; Cracking process; Acoustic emission; Digital image correlation

1. Introduction

The strength, deformation and crack behavior of rock materials are of great importance to rock mechanics and rock engineering. However, rock materials are naturally embedded with a variety of micro flaws, such as micro-cracks, micro-holes, fissures and joints. Due to the existence of these micro flaws, new cracks may initiate and propagate along these flaws under external loads. Furthermore, crack coalescence can lead to rock bridge failure, which makes a significant contribution to the failure of rock masse[1]. Therefore, the research on the mechanical properties and crack propagation behaviors is especially essential for the understanding of the failure mechanism of fissured rock and predicting geological hazards in rock engineering.

In order to investigate the failure mechanism of fissured rock, extensive experimental studies have been carried out for the mechanical behaviors of pre-existing fissured materials (rock-like material and real rock material)[2-6]. Due to the convenience of fabricating pre-existing fissures, rock-like materials have been widely applied in experimental studies. Shen investigated the mechanism of fracture coalescence of gypsum samples with two open or closed fissures under uniaxial compression and reported that coalescence can be caused by tensile crack, shear crack or mixed tensile and shear failure[2]. Bobet and Einstein carried out uniaxial and biaxial compression tests to investigate the influence of fissure geometry and the confining stress on the fracture behavior of gypsum samples with two fissures. Their experimental results showed that the type of crack coalescence was dependent on the fissure geometry[3]. Uniaxial compression tests on sandstone-like materials containing two parallel fissures were conducted by Wong and Chou[4]. Three typical modes, namely shear mode, mixed shear and tensile mode, and wing tensile mode were observed in their experiments. Afolagboye investigated the cracking behavior of moulded gypsum containing two non-parallel overlapping fissures under uniaxial compression[7]. Their study indicated that the geometry of pre-existing fissures affected crack initiation and coalescence behavior. When a specimen contains multiple pre-existing fissures, the crack initiation, propagation and coalescence behavior mainly depend on joint orientation and joint persistence[8]. Sagong and Bobet tested on a number of gypsum samples with three and sixteen fissures under uniaxial compression and found that the cracking pattern observed in specimens with multiple fissures was analogous to the pattern obtained in specimens with two fissures[9]. Zhou et al. carried out uniaxial compression tests for rock-like materials containing multiple fissures to research the effects of the layout of pre-existing fissures on mechanical properties, crack initiation modes and crack coalescence types[10]. Cao et al. tested on rock-like materials with two and three pre-existing fissures under uniaxial compression[11]. The experimental results showed that with the increase of the angle of the rock bridge, the rock specimen took a turn from wing crack propagation failure to crack coalescence failure. Nevertheless, it is difficult for rock-like materials to simulate all properties of real rock materials, although they can accurately simulate some properties.

For real rock materials, such as marble, granite, sandstone, limestone and shale, some intensive investigations have also been carried out. Wong et al. investigated the influences of fissure depths and fissure angles on crack propagation of marble specimens containing a single fissure[12]. It was found that the length of crack propagation depended on the ratio of the fissure depth to the thickness of the specimen. Lee and Jeon tested on granite specimens with two unparallel fissures under uniaxial compression and observed that a white patch took place before the crack initiated at that place, but cracks did not always appear at the place where the white patch emerged[13]. Yin et al. investigated the coalescence mechanism between two parallel three-dimensional pre-existing surface fissures in granite specimen under uniaxial compression. They found that the types of crack coalescence were dependent on the bridge angle[14]. In addition, a series of uniaxial compression tests for sandstone specimens containing a single fissure, two and three fissures were carried out[15-17]. They concluded that the crack behaviors of pre-cracked sandstone specimens mainly depended on the geometry of flaws, such as fissure angle, fissure length, ligament angle and ligament length. Furthermore, triaxial compression experiments on sandstone samples with two pre-existing non-overlapping flaws were performed to investigate the strength and deformation behaviors by Huang et al.[18]. They found a general rule that the arrangement of the flaw pair had greater impact on the rock deformation, strength and crack coalescence pattern than the confining pressure. Modiriasari et al. investigated the crack initiation, propagation and coalescence of Indiana limestone specimens with two pre-existing fissures under uniaxial compression using active seismic monitoring and digital image correlation[19]. Morgan and Einstein[20]] conducted a series of unconfined compression tests on prismatic shale specimens with two pre-existing fissures and various bedding plane orientations. It was found that as the bedding planes became more aligned with the direction of the maximum compressive stress the cracks initiating at the flaw tips propagated more frequently along the bedding planes.

In addition to experimental studies, numerical simulation studies on the failure mechanism of fissured rock have been widely conducted in parallel using various numerical methods, such as the boundary element method[21], finite element method[18,22], discontinuous deformation analysis[23], discrete element method[24-28], numerical manifold method[29], general particle dynamics[30,31], distinct lattice spring model[32], and rock failure process analysis[33, 34].

The aforementioned investigations have made an important contribution to the understanding of failure mechanism of fissured rock. However, fissure geometries in the above investigations were simplified. In practical engineering, rock materials are very complicated and fissures are commonly distributed randomly. **Figure 1** shows a natural rock mass containing pre-existing cross-fissures[35]. The interaction between these cross-fissures may lead to unstable failure of rock masses. Nevertheless, the interaction mechanism between cross-fissures has not been fully understood[35-37]. As a result, further investigations are urgently needed.

For this purpose, sandstone specimens containing cross-fissures were used for uniaxial compression tests in the present paper. Their mechanical behaviors and crack initiation, propagation and coalescence processes were investigated by means of stress-strain relationships, acoustic emission characteristics and digital images.

Figure 1. Cross-fissured rock mass[35].

2. Tested material and loading procedure

2.1. Sandstone material

The specimens used in this research are yellow sandstone samples with the size of 170 mm × 85 mm × 30 mm, as shown in **Figure 2a**. The cross-fissures were fabricated by a high pressure water jet cutting machine in the center of sandstone specimens. The geometry of them is defined by four geometric parameters: the length of fissure l_1, the fissure inclination angle α (the angle between fissure and horizontal axis), the ligament length l_2 (the distance between two cross points of fissures), and the ligament angle β (the angle between ligament and horizontal axis), as shown in **Figure 2b**. To investigate the influence of the fissures geometry on the strength and deformation behavior of sandstone under uniaxial compression, different geometries of cross-fissures were chosen for this research by varying the ligament angle from 0° to 90° at an interval of 15°, while keeping the other three parameters constant (l_1 = 22 mm, α= 45°, l_2 = 36 mm). Eight groups of specimens were prepared, and each of them includes two specimens. Before testing, the surface of specimens was evenly sprayed with black paint to create an artificial speckle field.

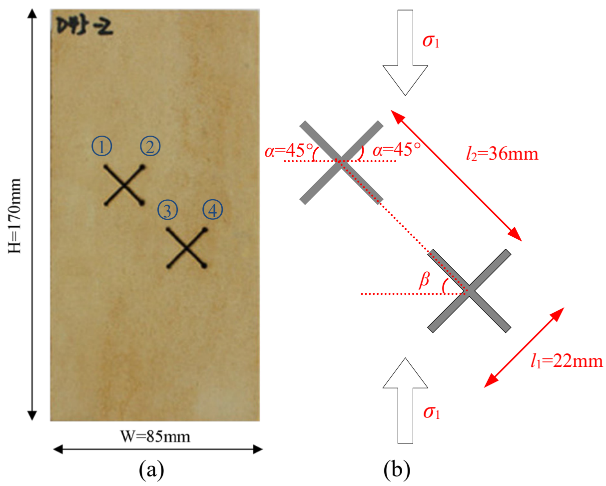

Figure 2. Geometry of cross-fissures in a sandstone specimen. (a) One typical specimen of D45-2. (b) Detailed geometry of cross-fissures.

2.2. Experimental system and loading procedure

Figure 3 shows the testing setup including loading system, acoustic emission system and three-dimensional digital image correlation (DIC) system. A servo-controlled rock mechanics machine (MTS816) was adopted in the loading system. The acoustic emission system employed an acoustic emission monitoring system (PCI-2) manufactured by USA physical acoustics company (PAC). The frequency of the acoustic emission system was set to 1 MHz. The XTDIC system, an optical non-contact three-dimensional deformation measurement system, was used to capture the images which were simultaneously stored on a computer for subsequent process in the DIC system. Uniaxial compression tests of the sandstone specimens were carried out using MTS816 at a constant displacement speed of 0.15 mm/min. During the test process, the acoustic emission signals and the digital images were recorded synchronously.

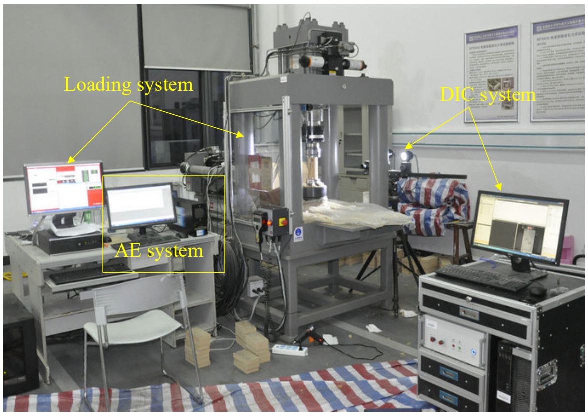

Figure 3. Experimental setup: MTS816 servo-controlled rock mechanics testing system, PCI-2 Acoustic Emission (AE) system and DIC system.

3. Strength and deformation behaviors

Figure 4 shows the uniaxial stress-strain curves of the two intact sandstone specimens. As shown in **Figure 4**, the loading process can be roughly divided into three stages. At the first stage, the specimens demonstrate nonlinear deformation behavior, which is mainly attributed to the closure of the original flaws in the specimens. At the second stage of loading, the specimens show elastic deformation behavior, i. e., the axial stress is in an approximately linear relation as the axial strain. With an increase of load, the specimens come into the stage of plastic compliance. After the peak strength, the axial stress drops sharply to zero, which reflects the brittleness of the tested sandstone specimen. In addition, we can also find that the stress-strain curves of the two intact specimens have a good agreement, to some extent indicating that the tested specimens are homogeneous.

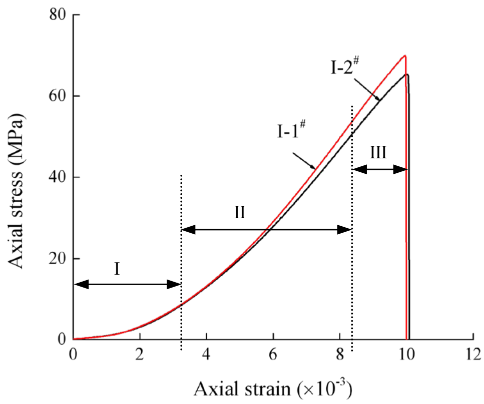

Figure 4. Stress-strain curves of intact sandstone specimens under uniaxial compression

Figure 5 shows the uniaxial stress-strain curves of the pre-cracked sandstone specimens with different ligament angles. As seen from **Figure 5**, the loading process can also be divided into three stages, similar to that of the intact specimens. Additionally, it is obviously found that for pre-cracked specimens with different ligament angles, the uniaxial stress-strain curves present different behaviors. Based on the analysis of characteristics, the uniaxial stress-strain curves can be classified into three categories, i. e. type A, type B and type C.

Type A ($0° \leq \beta \leq 30°, 75° \leq \beta \leq 90°$): for specimens with ligament angle of 0°, 15°, 30°, 75° and 90°, the stress drops sharply after the peak strength, indicating that these specimens fail in a transient mode.

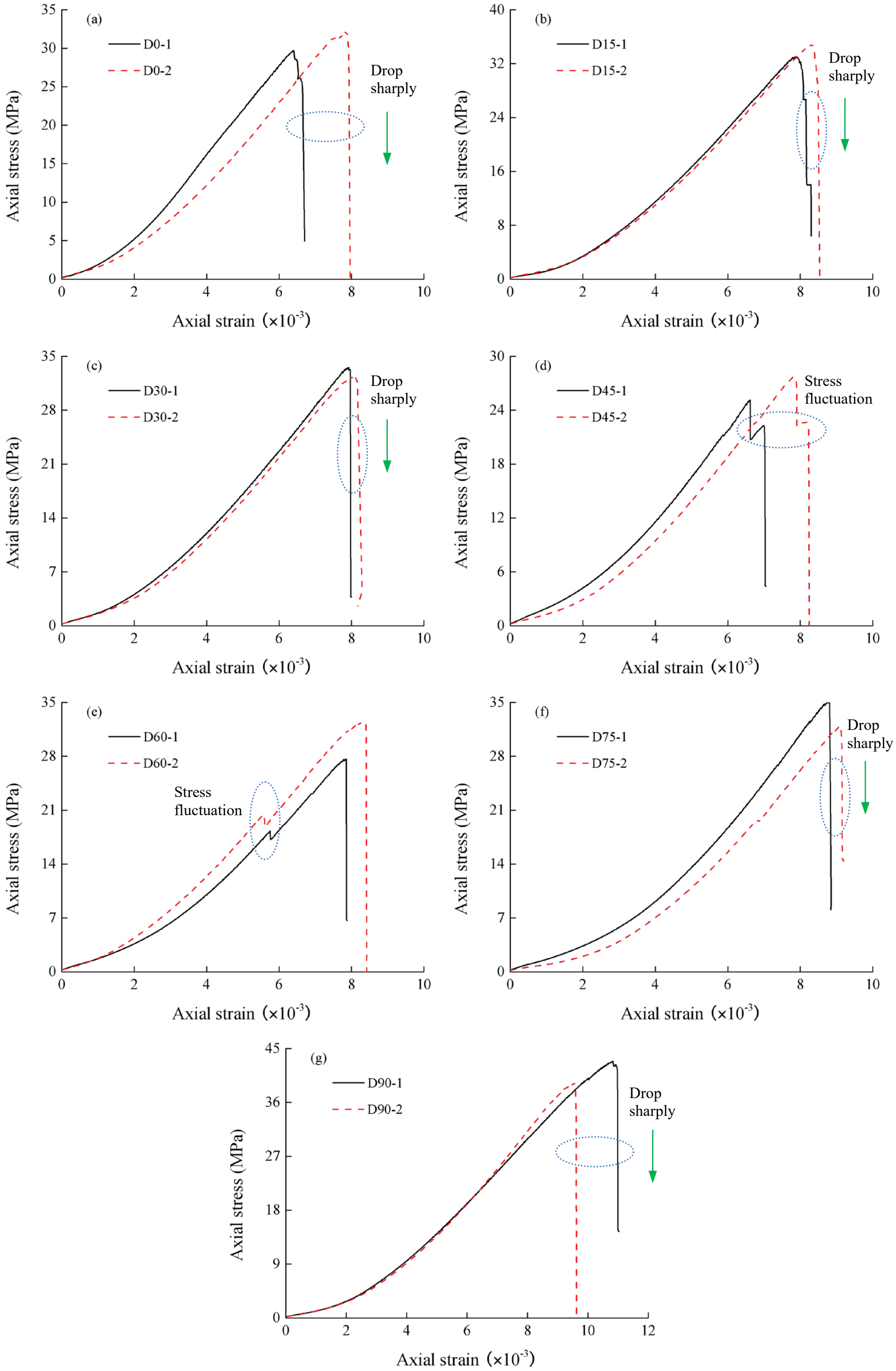

Figure 5. Uniaxial stress-strain curves of pre-cracked sandstone specimens with different ligament angles.

Type B (β=45°): for specimens with ligament angle of 45°, in contrast to type A, there is an obvious stress fluctuation point during post-peak process. It may be explained that new generated cracks enhance the friction coefficient of sliding face, resulting in a slight increase of strength for the pre-cracked sandstone specimen with ligament angle of 45°.

Type C (β=60°): for specimens with ligament angle of 60°, however, the most significant difference between type B and C is that stress fluctuation takes place in pre-peak stage. It can be speculated that a new crack may occur in the pre-cracked specimen with ligament angle of 60°.

Figure 6 shows the influence of the ligament angle on the strength and deformation properties of the pre-cracked sandstone specimens containing cross-fissures. In **Figure 6**, σ_p and ε_p are the uniaxial compressive strength and peak strain of the specimens, respectively, and E_s is the elastic modulus calculated in the range from 0.3σ_p to 0.7σ_p. As seen from **Figure 6a**, the peak strengths of the pre-cracked sandstone specimens first increase, and then decrease, finally increase again with the ligament angle, reaching the minimum value at β = 45°. With the ligament angle increasing from 0° to 15°, the average value of peak strength increases from 30.97 MPa to 33.97 MPa. However, as the ligament angle increases from 15° to 45°, the peak strength decreases from 33.97 MPa to 26.41 MPa. With the ligament angle increasing from 45° to 90°, the peak strength increases again from 26.41 MPa to 41.09 MPa. The relationship between the peak strain and the ligament angle is shown in **Figure 6b**. With the ligament angle increasing, the tendency of the peak strain is similar to that of the peak strength and the peak strain also reaches the lowest value (ε_p=7.22×10^{-3}) at β = 45°. Nevertheless, there is a slight difference in the trend between the peak strength and the peak strain. The lowest value of the peak strain also takes place at β = 0°. **Figure 6c** depicts the relationship between the elastic modulus and the ligament angle. The elastic modulus also reaches the minimum value (4.65 GPa) at β = 45°. In addition, we can find that the tendency of the elastic modulus with the ligament angle increasing is different from that of the peak strength and peak strain. As the ligament angle increases from 0° to 45°, the elastic modulus decreases from 5.60 GPa to 4.65 GPa. However, with the ligament angle increasing from 45° to 90°, the elastic modulus increases in turn from 4.65 GPa to 5.42 GPa.

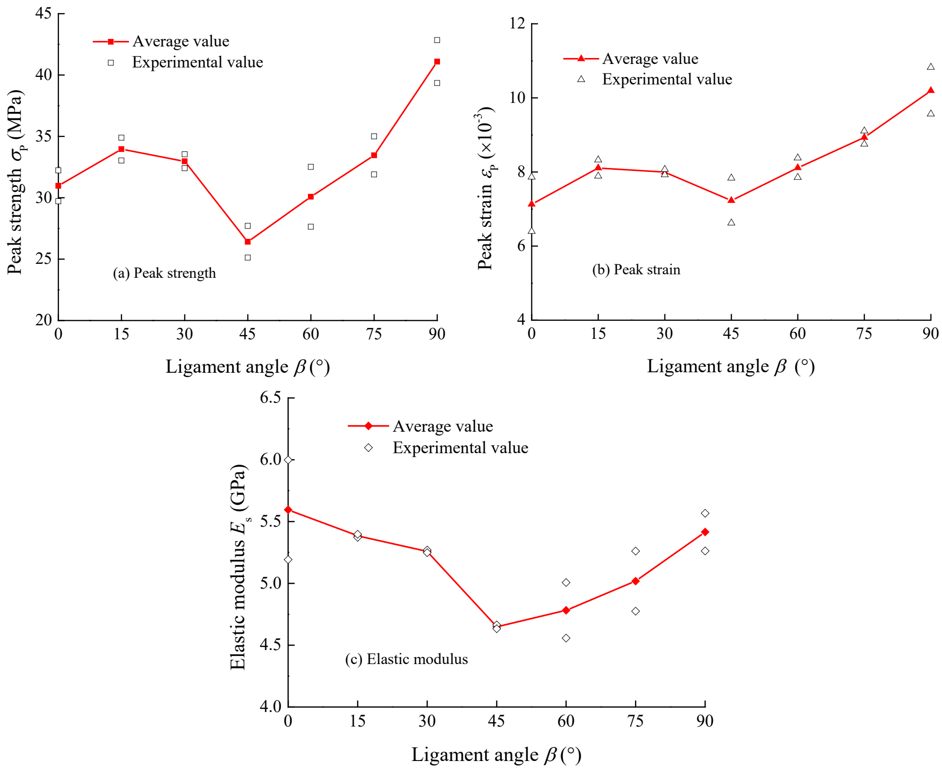

Figure 6 Influence of ligament angle on strength and deformation parameters of sandstone containing cross-fissures: (a) peak strength; (b) peak strain; (c) elastic modulus.

4. Fracture mechanism analysis

The failure mechanism of rock specimen can be well reflected by the strain localization zones on specimen surface[38]. Therefore, the strain localization zones of pre-cracked specimens with cross-fissures at different stress levels under uniaxial compression were analyzed to investigate the influences of different ligament angles on the fracture mechanism of pre-cracked specimens, combining the analysis of AE behaviors synchronously. Whereas similar failure patterns were observed for pre-cracked specimens with the same ligament angle, one typical specimen in each group was selected to be investigated in details as follows.

4.1. Failure modes and coalescence patterns of rock bridge

Figure 7 presents the ultimate failure modes of the pre-cracked sandstone specimens containing cross-fissures under uniaxial compression. In accordance with **Figure 7d~e,** we can determine that the failure patterns of the pre-cracked specimens with β = 45° are nearly the same, except for some slight differences, which also indicates that the tested specimens are so homogeneous that the influence of the heterogeneity of the specimens on the failure patterns can be neglected. It can be clearly seen that the failure mode of the pre-cracked specimen is closely related to the ligament angle. Based on the analysis of the failure modes, the main types of cracks can be divided into six categories, namely tensile crack, shear crack, lateral crack, wing crack, secondary crack, and surface spalling. As shown in **Figure 7c** and **Figure 7g**, the unnoticeable macro cracks in pre-cracked specimens are represented with white dotted lines.

Furthermore, it can be concluded that various ligament angles lead to different crack behaviors and crack types. As shown in **Figure 7**, the rock bridge coalescence patterns also mainly depend on the ligament angle. In comparison to the ultimate failure modes with different ligament angles, five types of rock bridge coalescence patterns can be indentified and summarized in **Table 1**. The unnoticeable macro cracks are denoted by white dotted lines in ultimate failure patterns, and correspondingly by semitransparent line in sketches of coalescence patterns, as illustrated in **Table 1**.

Type I: No coalescence

For the specimens with ligament angles of β = 0° and 15°, rock failure is formed mainly due to the coalescence of wing cracks initiated at cross-fissures tips, while no coalescence is observed in rock bridge area where only surface spalling takes place. As the rock bridge coalescence modes are almost the same, we select the specimen with β = 0° as a typical sample to illustrate this type. In the middle of the specimen, four triangle blocks are separated from the specimen by four tensile cracks initiated at the four fissures tips. A lateral crack generated at the left tip of fissure 1 extends to the left edge of the specimen. The explanation for this type may be that it is difficult for cracks to propagate in rock bridge area of specimens with small ligament angles.

Type II: Shear coalescence

This type of rock bridge coalescence mode can be observed in the specimens with ligament angles of β = 30° and 45°. In this paper, the specimen with β = 45° is taken as an example to be analyzed. As shown in **Table 1**, four triangle blocks are also separated from the specimen by four tensile cracks initiated at the four fissures tips. In sharp contrast, the rock bridge is coalesced by a secondary crack in the form of a shear crack linking the right tip of fissure 1 and the left tip of fissure 4. It can be explained that with an increase of the ligament angle, it becomes easy for cracks to propagate in rock bridge area.

Type III: Tensile coalescence

For the specimen with the ligament angle of β = 60°, the rock bridge area is also coalesced by single crack as presented in **Table 1**. However, the main distinction between this type of rock bridge coalescence and the above type is that the rock bridge area is coalesced by a tensile crack. In addition, there are only two triangle blocks formed as only two tensile cracks are generated. The reason for this type may be that the coalescence path between the right tip of fissure 1 and the left tip of fissure 3 is the shortest bridge and parallel to the direction of the maximum principal stress when the ligament angle equals 60°.

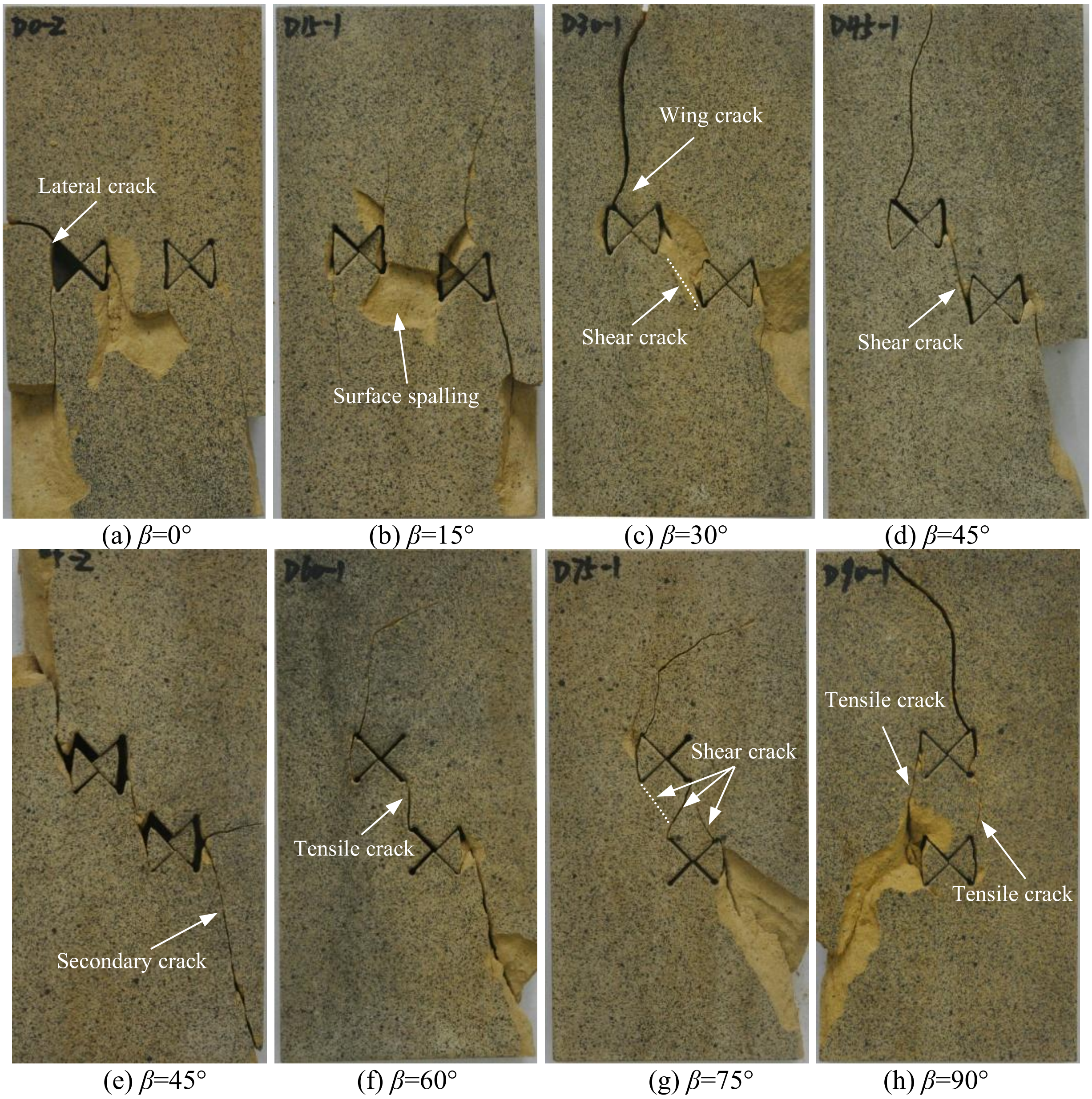

Figure 7. Ultimate failure patterns of the pre-cracked sandstone specimens containing cross-fissures.

Table 1. Rock bridge coalescence types and failure patterns of pre-cracked specimens with different ligament angles.

β	Coalescence types	Ultimate failure patterns	Sketches of coalescence pattern
0°, 15°	No coalescence	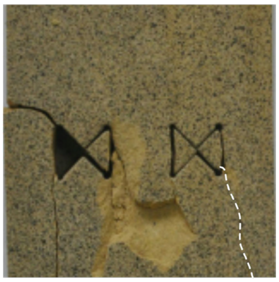	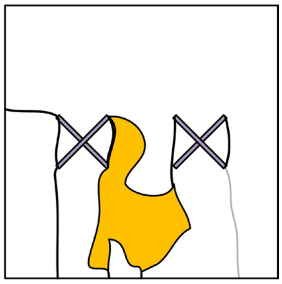
30°, 45°	S		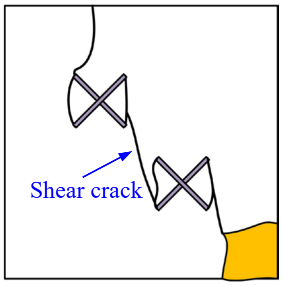
60°	T	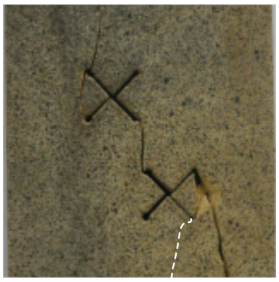	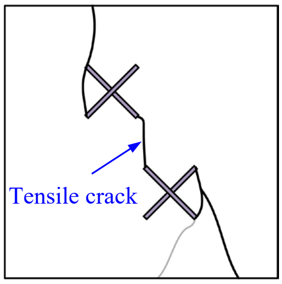
75°	T-S		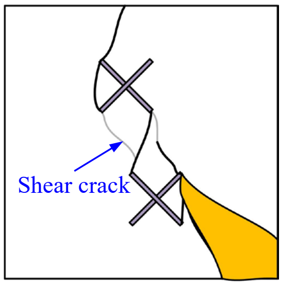
90°	D-T		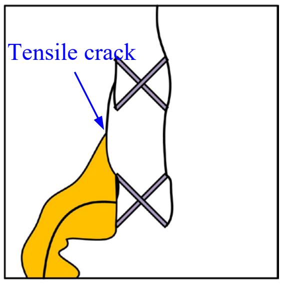

S: shear, T: tensile, T-S: three-shear, D-T: double-tensile

Type IV: Three-shear coalescence

This type of rock bridge coalescence mode is observed in the specimen with the ligament angle of $\beta = 75°$. As illustrated in **Table 1**, there are also only two triangle blocks generated, which is similar to the specimen with the ligament angle of $\beta = 60°$. Compared to the preceding types, the most evident difference for this type is that there are three rock bridge coalescence paths which are in the form of shear cracks. It can be speculated that with the ligament angle increasing, rock bridge coalescence path increases accordingly.

Type V: Double-tensile coalescence

For the specimen with the ligament angle of β = 90°, there are two coalescence paths in rock bridge area. In contrast to the above types, this type of rock bridge coalescence mode is double-tensile coalescence that is in the form of tensile cracks. Additionally, four triangle blocks are observed in the specimen again. Moreover, it is found that the rock bridge area is coalesced along the paths that are the shortest bridges when the ligament angle β equals 90°.

4.2. Cracking processes and strain field evolution

Analysis in Section 4.1 indicates that the failure modes and rock bridge coalescence patterns are closely related to the ligament angle. To investigate the failure mechanism of pre-cracked specimens with different ligament angles, cracking processes of specimens with ligament angle of 0°, 45°, 60°, 75° and 90° are analyzed combining with AE behaviors and strain field characteristics.

Figure 8 presents the axial stress-time curve, AE behaviors and the major principal strain field evolution of the specimen with ligament angle of β = 0°, including four critical stress points which are marked in the axial stress-time curve according to turning points in accumulated AE counts curve.

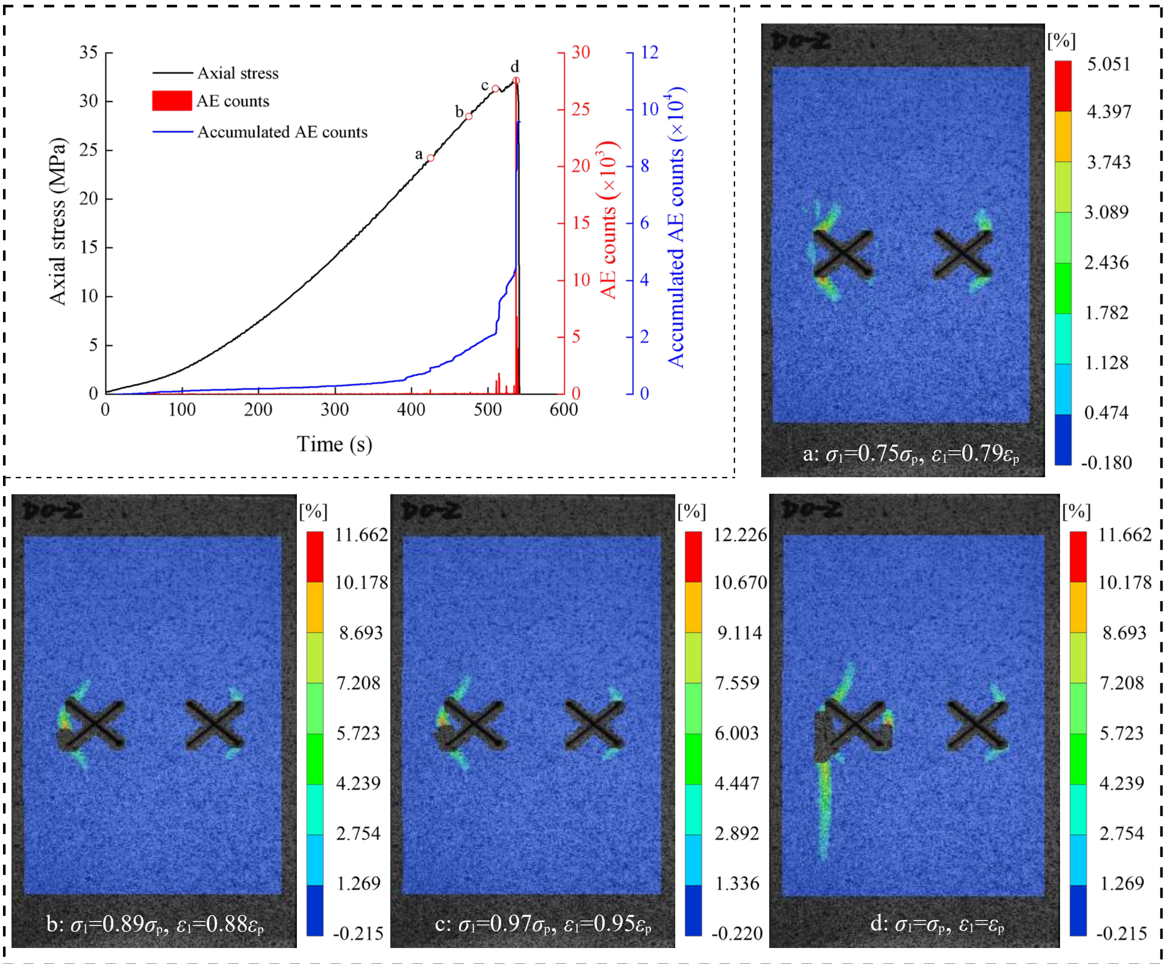

Figure 8. AE characteristic, uniaxial stress-time curve and the corresponding major principal strain field of pre-cracked specimen with ligament angle of 0°.

As shown in **Figure 8**, there are no obvious AE signals at the initial loading stage and no macro cracks are observed. With the axial stress increasing, the number of AE events increases steadily as shown in the accumulated AE counts curve. When the axial stress reaches to $0.75\sigma_p$, i. e. point (a) as marked in the axial stress-time curve, there is a turning point in accumulated AE counts curve. At the same time, four highlighted strain localization zones in the major principal strain field are observed at the left tips of fissure 1 and 2, and the right tips of fissure 3 and 4, respectively. The evolution of the strain localization zone can be used for identification of cracking processes, namely crack initiation, propagation and coalescence. At point (b), i. e. σ_1=$0.89\sigma_p$, a new highlighted strain localization zone is generated in the area between the left tips of fissure 1 and 2, which indicates that a macro crack might take place in the area. With an increase of the axial stress, AE signals become stronger and there is an obvious increase in the accumulated AE counts curve when the axial stress increases to $0.97\sigma_p$, i. e. point (c). Meanwhile, a slight stress drop is observed in the axial stress-time curve and a macro tensile crack is initiated at the left tip of fissure 2. The axial stress continues to increase until the peak value (32.22 MPa) is attained, namely point (d) as marked in the axial stress-time curve. At point (d), a tremendous increase in AE counts curve occurs and the tensile crack initiated at the left tip of fissure 2 is coalesced to link the left tip of fissure 1. A new long highlighted strain localization zone initiated at the left tip of fissure 2 propagates downwards along the direction of the major principal stress, which will subsequently evolve into a wing crack as shown in **Table 1**. In addition, another highlighted strain localization zone appears in the area between the right tips of fissure 1 and 2. Based on the above analysis, it can be speculated that the other macro cracks as illustrated in **Table 1** take place transiently after the peak strength.

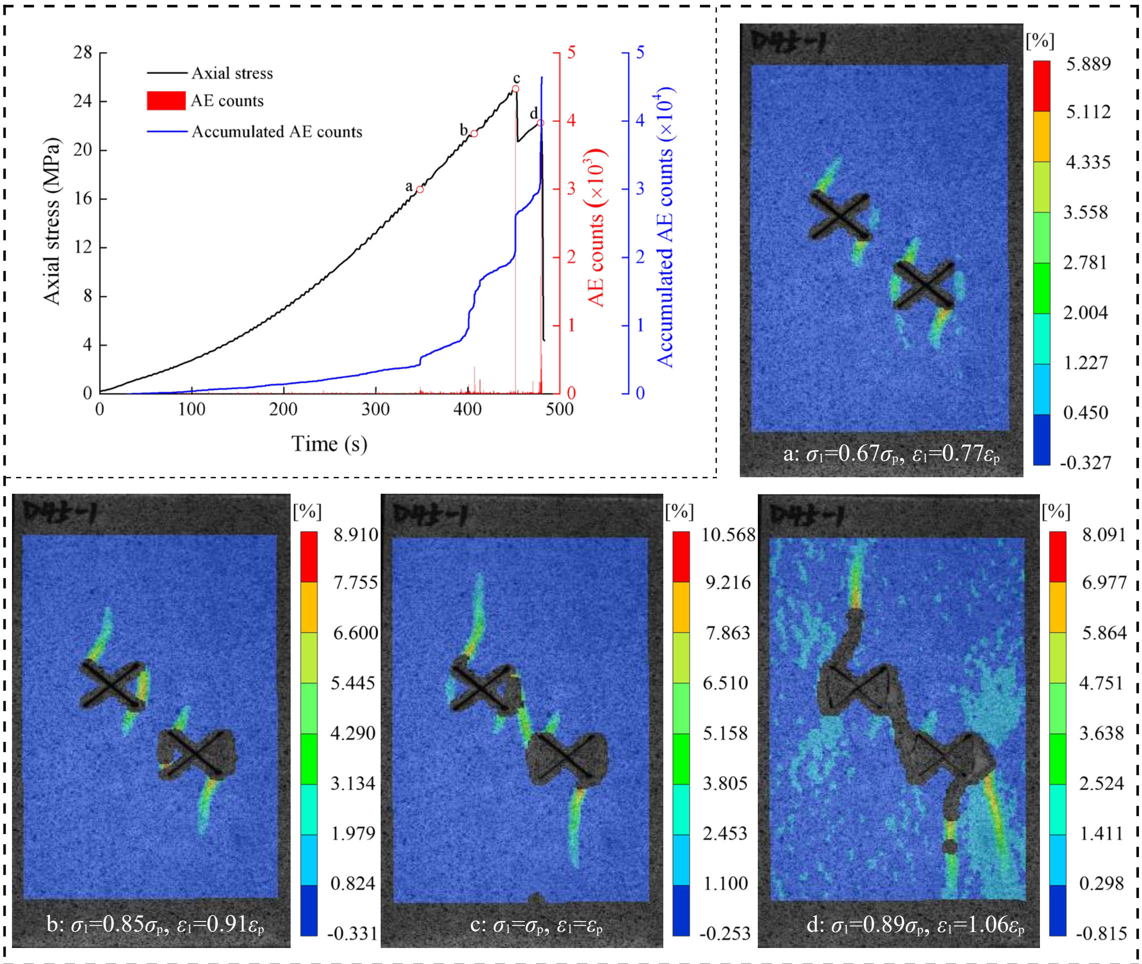

Figure 9. AE characteristic, uniaxial stress-time curve and the corresponding major principal strain field of pre-cracked specimen with ligament angle of 45°.

Figure 9 shows the axial stress-time curve, AE behaviors and the major principal strain field evolution of the specimen with ligament angle of β = 45°. In contrast to the above specimen, the number of AE events increases steadily as shown in the accumulated AE counts curve in the initial loading stage. Moreover, there is an obvious stress fluctuation point in the axial stress-time curve during the post-peak stage and the acoustic emission signals take place more densely and strongly, which indicates that the energy release of the sample becomes more serious. It is well known that energy dissipation and release play an important role in rock strength and deformation[39]. Based on the above analysis, it can be well explained for the foregoing conclusion that the peak strength of the pre-cracked sample reaches the minimum value at β = 45°. When the axial stress reaches to $0.67\sigma_p$, namely point (a), several highlighted strain localization zones are observed around the fissures tips. The first one initiated at the left tip of fissure 1 propagates upwards in the direction of the maximum principal stress. The second one initiated at the right tip of fissure 1 propagates downwards in the direction of the maximum principal stress. The third one grown at the left tip of fissure 3 and the forth one generated at the right tip of fissure 3 are similar to the first one and the second one, respectively. The other two strain localization zones are observed in the areas where link the left tips of fissure 1 and 2, and the right tips of fissure 3 and 4, respectively. At point (b), the axial stress and strain respectively reach to $0.85\sigma_p$ and $0.91\varepsilon_p$, i. e. 21.36 MPa and 5.92×10^{-3}. At this moment, as shown in **Figure 9**, there is a significant increase in AE counts curve and a new highlighted strain localization zone is observed in the area between the right tips of fissure 1 and 2. Additionally, the third strain localization zone and the forth one evolve into two tensile cracks. When the axial stress achieves the peak value (25.04 MPa), i. e. point (c) as marked in the axial stress-time curve, another new highlighted strain localization zone is observed in the vicinities of the right tip of fissure 1 and the left tip of fissure 3. It propagates obliquely and is an indication of rock bridge coalescence. After the peak strength, the axial stress drops sharply. However, there is an obvious stress fluctuation point during the post-peak stage, namely point (d). At point (d), the first strain localization zone initiated at the left tip of fissure 1 evolves into a wing crack and two tensile cracks are observed around the tips of fissure 1 and 2. Furthermore, the rock bridge area is coalesced by a shear crack and a new highlighted strain localization zone is generated at the right tip of fissure 3 that will propagate into a secondary crack later on as illustrated in **Table 1**. In addition, the strain localization zone initiated at the right tip of fissure 3 evolves into a wing crack and continues to propagate downwards along the direction of the maximum principal stress.

Figure 10 demonstrates the axial stress-time curve, AE behaviors and the major principal strain field evolution of the specimen with ligament angle of β = 60°. As seen from **Figure 10**, there are several obvious distinctions in AE behaviors between this specimen and the above specimens. The first one is that a stress fluctuation point takes place in the pre-peak stage and meanwhile a sharp increase occurs in AE counts curve. The second one is that two tremendous increasing points in AE counts curve are observed during the pre-peak stage. With the ligament angle increasing, great changes in the evolution pattern of the major principal strain field also take place. At point (a), i. e. $\sigma_1=0.66\sigma_p$, several highlighted strain localization zones are generated in the vicinities of the fissures tips. The first one is initiated at the left tip of fissure 1 and propagates upwards in the direction of the major principal stress. At the right tip of fissure 1, two highlighted strain localization zones are generated, and one of them is perpendicular to the fissure 1 and the other propagates downwards along the direction of the maximum principal stress. At the left tip of fissure 3, a highlighted strain localization zone is also observed, which is perpendicular to the fissure 3. At the right tip of fissure 3, a new highlighted strain localization zone is initiated perpendicular to the fissure 3 and turns to propagate downwards in the direction of the major principal stress with the axial stress increasing. We can also find that there is a strain localization zone in the area between the right tips of fissure 3 and 4 although it is slightly weak. At point (b), i. e. $\sigma_1=0.84\sigma_p$, there is a sharp increase in AE counts curve and the strain localization zone in rock bridge area becomes more highlighted, which will subsequently evolve into a tensile crack when the axial increases to $0.94\sigma_p$, namely point (c). At point (c), there is a turning point in the accumulated AE counts curve and a new highlighted strain localization zone is generated in the area between the left tips of fissure 1 and 2.. In addition, a macro tensile crack is observed in the area between the right tips of fissure 3 and 4. When the axial stress and strain respectively reach the peak values (27.64 MPa and 7.85×10^{-3}), i. e. point (d) marked in axial stress-time curve in **Figure 10**, AE counts reach the peak value (2.16×10^{3}) and a new strain localization zone takes place at the right tip of fissure 3 and propagates downwards along the direction of the maximum principal stress, which will evolve into a secondary crack later on as shown in **Table 1**.

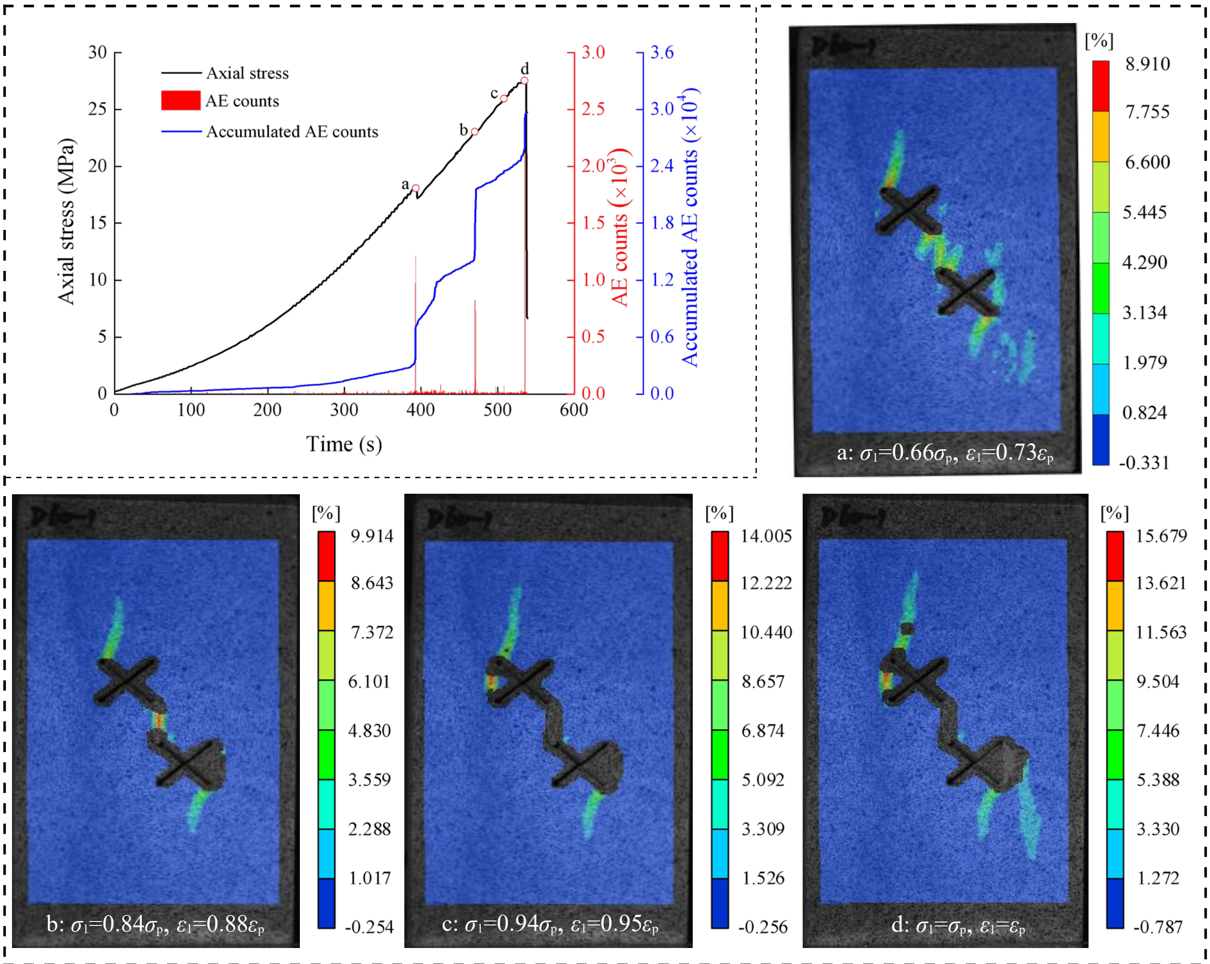

Figure 10. AE characteristic, uniaxial stress-time curve and the corresponding major principal strain field of pre-cracked specimen with ligament angle of 60°.

Figure 11 shows the axial stress-time curve, AE behaviors and the major principal strain field evolution of the specimen with ligament angle of β = 75°. Compared with **Figure 10** and **Figure 11**, there are some similarities in AE behaviors. Two tremendous increasing points are also observed in AE counts curve during the pre-peak stage and the peak value of AE counts is also attained at the peak strength. However, there are several significant differences in the evolution of the major principal strain field between the two specimens. As illustrated in **Figure 11**, there is a sharp increase in AE counts curve when the axial stress reaches to $0.76\sigma_p$, i. e. point (a) marked in the axial stress-time curve. At point (a), some highlighted strain localization zones are initiated at the fissures tips. The first one initiated at the left tip of fissure 1 is perpendicular to the fissure 1 and turns to propagate upwards along the direction of the maximum principal stress. At the left tip of fissure 2, a new highlighted strain localization zone is observed, which is perpendicular to the fissure 2. At the right tip of fissure 4, two highlighted strain localization zones are generated. One of them is perpendicular to the fissure 4 and the other extends downwards in the direction of the maximum principal stress to the right tip of fissure 3. At point (b), i. e. σ_1=$0.92\sigma_p$, a significant increase takes place in AE counts curve and a new strain localization zone is grown in the area between the left tips of fissure 1 and 2, which will propagate into a macro tensile crack when the axial stress reaches to $0.98\sigma_p$, namely point (c). At point (c), a long and thick strain localization zone is generated at the right tip of fissure 3 and propagates obliquely to the lower-right edge of the sample. When the axial stress reaches the peak value (34.99 MPa), i. e. point (d), the major principal strain field pattern is almost the same as that at point (c) except for the maximum principal strain value. Based on the previous analysis in Section 4.1, however, there is a macro shear crack in the area between the right tip of fissure 1 and the left tip of fissure 3, which makes a significant contribution to the coalescence of rock bridge area. It can be explained that the rock bridge area is coalesced instantly and there is no time to capture the failure image at that moment.

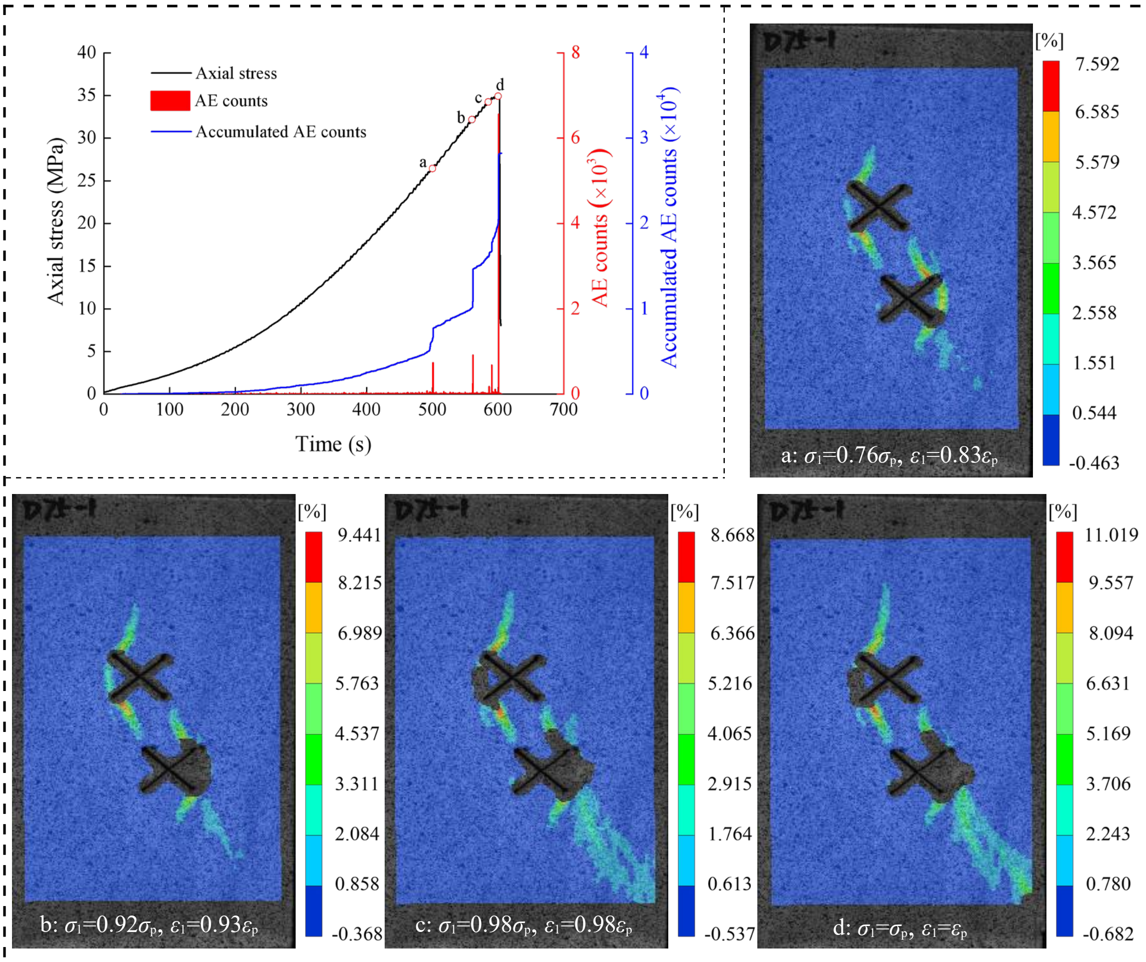

Figure 11. AE characteristic, uniaxial stress-time curve and the corresponding major principal strain field of pre-cracked specimen with ligament angle of 75°.

Figure 12 displays the axial stress-time curve, AE behaviors and the major principal strain field evolution of the specimen with ligament angle of $\beta = 90°$. In contrast to the above analyzed samples, there is an obvious difference in AE behaviors, which is that the peak value of AE counts is attained at the post-peak stage. Based on the above analysis, it can be concluded that AE counts reach the maximum value at or after the peak strength. In addition, there are also some differences in the evolution of the major principal strain field. At point (a), the axial stress reaches to $0.72\sigma_p$ and a significant increase takes place in AE counts curve. Four highlighted strain localization zones are generated at the tips of fissure 2 and 4, respectively. There are also some weak strain localization zones initiated at the tips of fissure 1 and 3. At the following point (b), i. e. $\sigma_1=0.93\sigma_p$, there is an obvious increase in AE counts curve and a macro tensile crack is observed in the area between the left tips of fissure 1 and 2. In addition, a highlighted strain localization zone propagates to link the right tips of fissure 1 and 4 in rock bridge area. Two highlighted strain localization zones are further enhanced in the areas between the tips of fissure 3 and 4. When the axial stress reaches the peak value (42.84 MPa), namely point (c), a new highlighted strain localization zone is generated and propagates to link the left tips of fissure 2 and 3 in rock bridge area. At point (d), the axial stress declines to $0.98\sigma_p$ and AE counts reach the peak value. Two highlighted strain localization zones in rock bridge area are further enhanced and will evolve into two macro tensile cracks as illustrated in **Table 1**. Additionally, a macro shear crack is initiated at the left-lower edge of the specimen, where a strain localization zone is generated. The strain localization zone propagates obliquely upwards and will subsequently evolve into a shear crack as shown in **Table 1**.

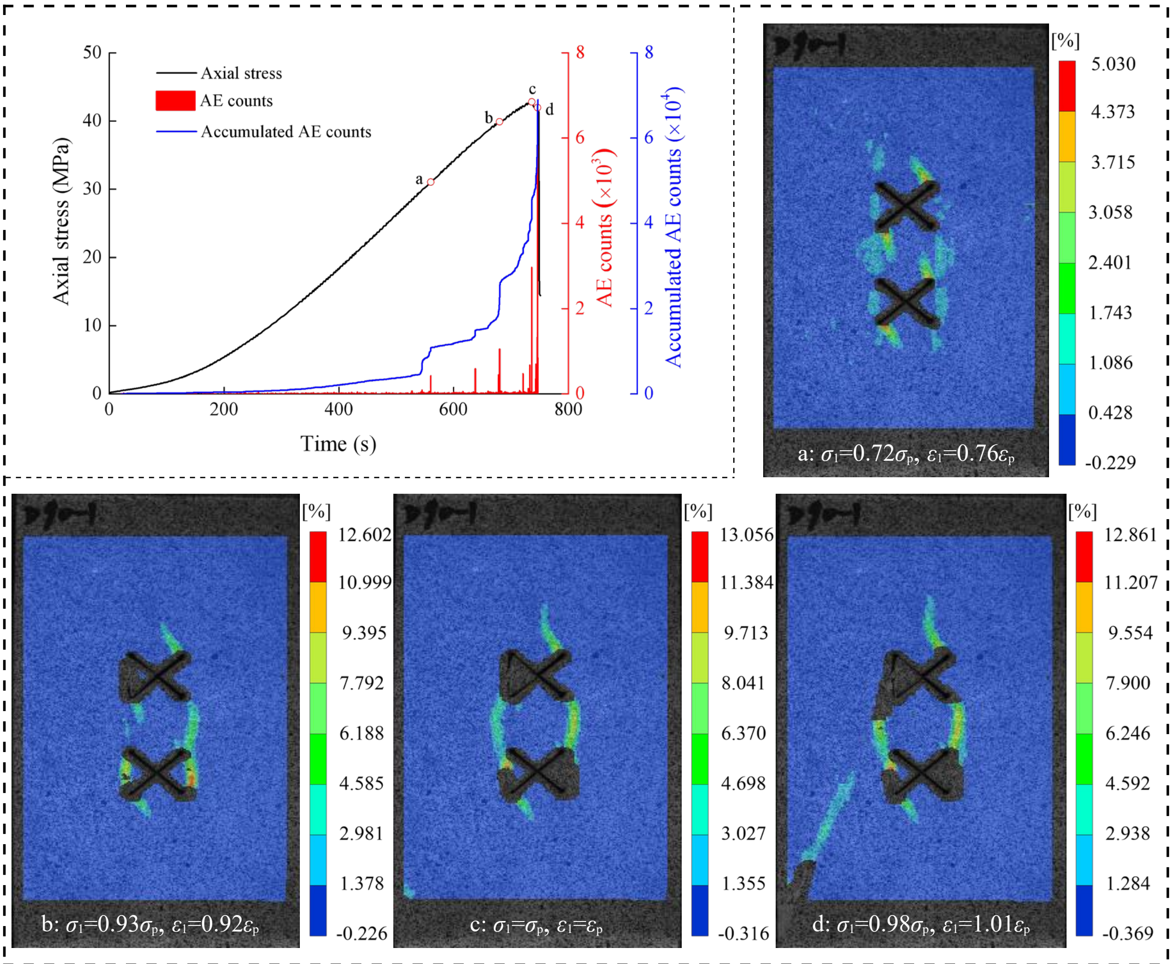

Figure 12. AE characteristic, uniaxial stress-time curve and the corresponding major principal strain field of pre-cracked specimen with ligament angle of 90°.

5. Conclusions

In the current work, the mechanical properties and failure mechanism of pre-cracked sandstone specimens with various ligament angles are investigated by uniaxial compression tests. The main conclusions have been drawn as follows:

(1) In accordance to the stress regimes of pre-cracked specimens with different ligament angles, the uniaxial stress-strain curves can be divided into three categories. With the ligament angle increasing, the peak strength and peak strain first increase, and then decrease, finally increase again, whereas the elastic modulus first decreases and then increases. When the ligament angle β equals 45°, the peak strength, peak strain and elastic modulus all reach the minimum value.

(2) The ultimate failure patterns of pre-cracked specimens are closely related to the ligament angle. In com-

parison to the ultimate failure modes with different ligament angles, five types of rock bridge coalescence mode can be identified, namely no coalescence, shear coalescence, tensile coalescence, three-shear coalescence and double-tensile coalescence.

(3) The relationships between the stress states, AE behaviors and strain field characteristics have been investigated in details. AE counts reach the maximum value at or after the peak strength. The evolution of the strain localization zone can be used for identification of cracking processes, namely crack initiation, propagation and coalescence.

Author Contributions

Xiang-Ru Liu, Yuan-Yuan Wan and Xue-Lei Zhang conceived and designed the experiments; Xiang-Ru Liu and Xue-Lei Zhang performed the experiments; Xiang-Ru Liu wrote the paper; Yuan-Yuan Wan revised the paper.

Acknowledgements

The work presented in this paper was supported by Higher Education Institutions Innovation and Entrepreneurship Training Program for College Students in Jiangsu Province (202414160098Y) and Suqian Sci&Tech Program (K202240). The authors would like to express their sincere gratitude for this support.

Conflicts of Interest

The authors declare no conflict of interest.

References

[1] Lajtai, E. Z. Brittle fracture in compression. Int J Fract. 1974, 10, 525-536. https://doi. org/10.1007/BF00155255

[2] Shen, B. The mechanism of fracture coalescence in compression-experimental study and numerical simulation. Eng Fract Mech. 1995, 51, 73-85. https://doi. org/10.1016/0013-7944(94)00201-R

[3] Bobet, A.; Einstein, H. H. Fracture coalescence in rock-type materials under uniaxial and biaxial compression. Int J Rock Mech Min Sci. 1998, 35, 863-889. https://doi. org/10.1016/S0148-9062(98)00005-9

[4] Wong, R. H. C.; Chau, K. T. Crack coalescence in a rock-like material containing two cracks. Int J Rock Mech Min Sci. 1998, 35, 147-164. https://doi. org/10.1016/S0148-9062(97)00303-3

[5] Li, Y.-P.; Chen, L.-Z.; Wang, Y.-H. Experimental research on pre-cracked marble under compression. Int J Solids Struct. 2005, 42, 2505-2516. http://dx. doi. org/10.1016/j. ijsolstr.2004.09.033

[6] Hall, S. A.; Sanctis, F. d.; Viggiani, G. Monitoring fracture propagation in a soft rock (Neapolitan Tuff) using acoustic emissions and digital images. Pure Appl Geophys. 2006, 163, 2171-2204. http://dx. doi. org/10.1007/s00024-006-0117-z

[7] Afolagboye, L. O.; He, J.; Wang, S. Experimental study on cracking behaviour of moulded gypsum containing two non-parallel overlapping flaws under uniaxial compression. Acta Mech Sin. 2017, 33, 394-405. http://dx. doi. org/10.1007/s10409-016-0624-9

[8] Chen, X.; Liao, Z. H.; Peng, X. Cracking process of rock mass models under uniaxial compression. J Cent South Univ. 2013, 20, 1661-1678. http://dx. doi. org/10.1007/s11771-013-1660-2

[9] Sagong, M.; Bobet, A. Coalescence of multiple flaws in a rock-model material in uniaxial compression. Int J Rock Mech Min Sci. 2002, 39, 229-241. https://doi. org/10.1016/S1365-1609(02)00027-8

[10] Zhou, X. P.; Cheng, H.; Feng, Y. F. An experimental study of crack coalescence behaviour in rock-like materials containing multiple flaws under uniaxial compression. Rock Mech Rock Eng. 2014, 47, 1961-1986.

http://dx. doi. org/10.1007/s00603-013-0511-7
[11] Cao, P.; Liu, T.; Pu, C.; Lin, H. Crack propagation and coalescence of brittle rock-like specimens with pre-existing cracks in compression. Eng Geol. 2015, 187, 113-121. http://dx. doi. org/10.1016/j. enggeo.2014.12.010
[12] Wong, R. H. C.; Law, C. M.; Chau, K. T.; Zhu, W. S. Crack propagation from 3-D surface fractures in PMMA and marble specimens under uniaxial compression. Int J Rock Mech Min Sci. 2004, 41, 37-42. http://dx. doi. org/10.1016/j. ijrmms.2004.03.016
[13] Lee, H.; Jeon, S. An experimental and numerical study of fracture coalescence in pre-cracked specimens under uniaxial compression. Int J Solids Struct. 2011, 48, 979-999. http://dx. doi. org/10.1016/j. ijsolstr.2010.12.001
[14] Yin, P.; Wong, R. H. C.; Chau, K. T. Coalescence of two parallel pre-existing surface cracks in granite. Int J Rock Mech Min Sci. 2014, 68, 66-84. http://dx. doi. org/10.1016/j. ijrmms.2014.02.011
[15] Yang, S. Q. Crack coalescence behavior of brittle sandstone samples containing two coplanar fissures in the process of deformation failure. Eng Fract Mech. 2011, 78, 3059-3081. http://dx. doi. org/10.1016/j. engfracmech.2011.09.002
[16] Yang, S. Q.; Jing, H. W. Strength failure and crack coalescence behavior of brittle sandstone samples containing a single fissure under uniaxial compression. Int J Fract. 2011, 168, 227-250. http://dx. doi. org/10.1007/s10704-010-9576-4
[17] Yang, S. Q.; Yang, D. S.; Jing, H. W.; Li, Y. H.; Wang, S. Y. An experimental study of the fracture coalescence behaviour of brittle sandstone specimens containing three fissures. Rock Mech Rock Eng. 2012, 45, 563-582. http://dx. doi. org/10.1007/s00603-011-0206-x
[18] Huang, D.; Gu, D.; Yang, C.; Huang, R.; Fu, G. Investigation on mechanical behaviors of sandstone with two preexisting flaws under triaxial compression. Rock Mech Rock Eng. 2015, 49, 375-399. http://dx. doi. org/10.1007/s00603-015-07573
[19] Modiriasari, A.; Bobet, A.; Pyrak-Nolte, L. J. Active seismic monitoring of crack initiation, propagation, and coalescence in rock. Rock Mech Rock Eng. 2017, 50, 2311-2325. http://dx. doi. org/10.1007/s00603-017-1235-x
[20] Morgan, S. P.; Einstein, H. H. Cracking processes affected by bedding planes in Opalinus shale with flaw pairs. Eng Fract Mech. 2017, 176, 213-234. http://dx. doi. org/10.1016/j. engfracmech.2017.03.003
[21] Steen, B. V. D.; Vervoort, A.; Napier, J. A. L. Numericalmodelling of fracture initiation and propagation in biaxial tests on rock samples. Int J Fract. 2001, 108, 165-191. https://doi. org/10.1023/A:1007697120530
[22] Fu, J.-W.; Zhang, X.-Z.; Zhu, W.-S.; Chen, K.; Guan, J.-F. Simulating progressive failure in brittle jointed rock masses using a modified elastic-brittle model and the application. Eng Fract Mech. 2017, 178, 212-230. http://dx. doi. org/10.1016/j. engfracmech.2017.04.037
[23] Huang, D.; Song, Y.; Cen, D.; Fu, G. Numerical modeling of earthquake-induced landslide using an improved discontinuous deformation analysis considering dynamic friction degradation of joints. Rock Mech Rock Eng. 2016, 49, 4767-4786. http://dx. doi. org/10.1007/s00603-016-1056-3
[24] Farahmand, K.; Vazaios, I.; Diederichs, M. S.; Vlachopoulos, N. Investigating the scale-dependency of the geometrical and mechanical properties of a moderately jointed rock using a synthetic rock mass (SRM) approach. Comput Geotech. 2018, 95, 162-179. http://dx. doi. org/10.1016/j. compgeo.2017.10.002
[25] Zhang, X.-P.; Zhang, Q.; Wu, S. Acoustic emission characteristics of the rock-like material containing a single flaw under different compressive loading rates. Comput Geotech. 2017, 83, 83-97. http://dx. doi. org/10.1016/j. compgeo.2016.11.003
[26] Liu, J.; Wang, J. Stress evolution of rock-like specimens containing a single fracture under uniaxial loading: a numerical study based on particle flow code. Geotech Geol Eng. 2017, 36, 567-580. http://dx. doi. org/10.1007/s10706-017-0347-0

[27] Turichshev, A.; Hadjigeorgiou, J. Development of synthetic rock mass bonded block models to simulate the behaviour of intact veined rock. Geotech Geol Eng. 2016, 35, 313-335. http://dx. doi. org/10.1007/s10706-016-0108-5

[28] Duriez, J.; Scholtès, L.; Donzé, F. V. Micromechanics of wing crack propagation for different flaw properties. Eng Fract Mech. 2016, 153, 378-398. http://dx. doi. org/10.1016/j. engfracmech.2015.12.034

[29] Zhou, X.; Fan, L.; Wu, Z. Effects of microfracture on wave propagation through rock massmass. Int J Geomech. 2017, 17, 072-085. http://dx. doi. org/10.1061/(ASCE)GM.1943-5622.0000947.©2017

[30] Zhou, X. P.; Shou, Y. D. Numerical simulation of failure of rock-like material subjected to compressive loads using improved peridynamic method. Int J Geomech. 2017, 17, 086-097. http://dx. doi. org/10.1061/(ASCE)GM.1943-5622.0000778.©2016

[31] Zhou, X. P.; Bi, J.; Qian, Q. H. Numerical simulation of crack growth and coalescence in rock-like materials containing multiple pre-existing flaws. Rock Mech Rock Eng. 2015, 48, 1097-1114. http://dx. doi. org/10.1007/s00603-014-0627-4

[32] Zhao, G.-F.; Lian, J.-J.; Russell, A. R.; Zhao, J. Three-dimensional DDA and DLSM coupled approach for rock cutting and rock penetration. Int J Geomech. 2017, 17, 015-031. http://dx. doi. org/10.1061/(ASCE)GM.1943-5622.0000754.©2016

[33] Yu, Q.; Yang, S.; Ranjith, P. G.; Zhu, W.; Yang, T. Numerical modeling of jointed rock under compressive loading using x-ray computerized tomography. Rock Mech Rock Eng. 2015, 49, 877-891. http://dx. doi. org/10.1007/s00603-015-0800-4

[34] Wong, R. H. C.; Tang, C. A.; Chau, K. T.; Lin, P. Splitting failure in brittle rocks containing pre-existing flaws under uniaxial compression. Eng Fract Mech. 2002, 69, 1853-1871. http://dx. doi. org/10.1016/S0013-7944(02)00065-6

[35] Cao, R.-H.; Cao, P.; Fan, X.; Xiong, X.; Lin, H. An experimental and numerical study on mechanical behavior of ubiquitous-joint brittle rock-like specimens under uniaxial compression. Rock Mech Rock Eng. 2016, 49, 4319-4338. http://dx. doi. org/10.1007/s00603-016-1029-6

[36] Zhang, B.; Li, S.; Xia, K.; Yang, X.; Zhang, D.; Wang, S.; Zhu, J. Reinforcement of rock mass with cross-flaws using rock bolt. Tunn Undergr Sp Tech. 2016, 51, 346-353. http://dx. doi. org/10.1016/j. tust.2015.10.007

[37] Yin, Q.; Jing, H.; Zhu, T. Mechanical behavior and failure analysis of granite specimens containing two orthogonal fissures under uniaxial compression. Arab J Geosci. 2015, 9, 2078-2092. http://dx. doi. org/10.1007/s12517-015-2078-y

[38] Li, D.; Zhu, Q.; Zhou, Z.; Li, X.; Ranjith, P. G. Fracture analysis of marble specimens with a hole under uniaxial compression by digital image correlation. Eng Fract Mech. 2017, 183, 109-124. http://dx. doi. org/10.1016/j. engfracmech.2017.05.035

[39] Peng, R.; Ju, Y.; Wang, J. G.; Xie, H.; Gao, F.; Mao, L. Energy dissipation and release during coal failure under conventional triaxial compression. Rock Mech Rock Eng. 2015, 48, 509-526. http://dx. doi. org/10.1007/s00603-014-0602-0